Journal of Materials Chemistry A

Fabrication of Freestanding Metal Organic Framework Predominant Hollow Fiber Mat and Its Potential Applications in Gas Separation and Catalysis

Journal:	*Journal of Materials Chemistry A*
Manuscript ID	TA-ART-10-2019-011701.R1
Article Type:	Paper
Date Submitted by the Author:	17-Jan-2020
Complete List of Authors:	Dai, Zijian; North Carolina State University, Chemical and Biomolecular Engineering; Donghua University Lee, Dennis; North Carolina State University, Chemical and Biomolecular Engineering Shi, Kaihang; North Carolina State University, Chemical & Biomolecular Engineering Wang, Siyao; North Carolina State University, Chemical and Biomolecular Engineering Barton, Heather; North Carolina State University, Chemical & Biomolecular Engineering Zhu, Jie; Shanghai University of Engineering Science Yan, Jiaqi; North Carolina State University, Chemical and Biomolecular Engineering Ke, Qinfei; Donghua University Parsons, Gregory; North Carolina State University, Chemical and Biomolecular Engineering

Journal of

Materials Chemistry A

Paper

Received 00th January 20xx,
Accepted 00th January 20xx

DOI: 10.1039/x0xx00000x

www.rsc.org/

Fabrication of Freestanding Metal Organic Framework Predominant Hollow Fiber Mat and Its Potential Applications in Gas Separation and Catalysis

Zijian Dai [a, b], Dennis T. Lee [b], Kaihang Shi [b], Siyao Wang [b], Heather F. Barton [b], Jie Zhu [c], Jiaqi Yan [b], Qinfei Ke [a, *], and Gregory N. Parsons [b, *]

Recently, metal-organic frameworks (MOFs) based polymeric substrates show promising performance in many engineering and technology fields. However, a common known drawback of MOF/polymer composite is MOF crystal encapsulation and reduced surface area. This work reports on a facile and gentle strategy to produce self-supported MOF predominant hollow fiber mats. A wide range of hollow MOFs including, MIL-53(Al)-NH_2, Al-PMOF, and ZIF-8 are successfully fabricated by our synthetic method. The synthetic strategy combines atomic layer deposition (ALD) of metal oxides to polymer fibers and subsequent selective removal of polymer components followed by conversion of remaining hollow metal oxides into freestanding MOF predominant hollow fiber structures. The hollow MOFs show boosted surface area, superb porosity, excellent pore accessibility, and exhibit a significantly improved performance in CO_2 adsorption (3.30 mmol g^{-1}), CO_2/N_2 separation seletivity (15/85 and 50/50 CO_2/N_2 mixtures are 24.9 and 21.2), and catalytic removal of HCHO (complete oxidation of 150 ppm within 60 min).

Introduction

Metal-organic-frameworks (MOFs) are highly crystalline and porous materials consisting of metal ions or clusters which are coordinated with organic linkers.[1, 2]Impressive progress has been made using MOFs in gas storage and separation,[3, 4] volatile organic compound (VOC) adsorption,[5-7] heterogeneous catalysis,[8-15] and environmental decontamination.[16] These advances result from unique advantages of MOFs, such as controllable pore size, high surface areas and porosity, well-dispersed active centers, and tailorable functionalities.

Because MOF powders are difficult to handle and utilize,[17] significant research effort is focused on integrating MOFs into robust MOF-fibers,[18, 19] and membranes.[20, 21] A polymer fiber or membrane provides mechanical support and can substantially reduce MOF aggregation, leads to improvement in functional performance on a per-gram of MOF basis. MOF/fiber composites have shown marked advantages in catalysis,[22] pollution control,[23] gas separation,[24] and sensing[25] applications. Moreover, MOF/fiber composites enable more than one type of MOFs to be coupled together to simultaneously perform multiple functions.[19]

Despite the reported advances in MOF polymer composites, there are several common challenges to create high performance structures. For example, during formation, polymer from the fiber can infuse or otherwise unfavorably interact with the MOF to block pore access.[26] Also, for biomedical applications, biocompatible polymers (e.g., polyvinylpyrrolidone, polyvinylalcohol, poly(lactic-co-glycolic acid), and gelatin)[27] must be used to construct the MOF polymer composites, thereby limiting the substrate selection.

While several groups have demonstrated MOF/fiber composites, very few reports describe approaches to produce free-standing MOF fiber mats or provide quantified functional performance of the products. Li and coauthors reported a strategy applying soft ceramic oxide fibers as MOF conversion templates, and suggested that resulting MOF fibers would retain the original fiber flexibility and softness.[26, 28] Dwyer et al., demonstrated a unique synthetic approach to create hollow TiO_2 cylinders with dense MOF crystals on the inner and outer surfaces.[29] These methods possess some drawbacks such as low surface area, and time- and energy-consuming material processing.

Here, we report on a facile and unique approach to synthesize freestanding MOF enriched hollow structures via oxide-to-MOF conversion, also known as coordination replication.[30, 31] The metal oxides used here, Al_2O_3 and ZnO, are formed conformally on starting polymer fibers using low-temperature atomic layer deposition (ALD).[18, 19, 22 32] These oxides allow successful synthesis of MIL-53(Al)-NH_2, Al-PMOF, and ZIF-8 MOFs. In this work, cellulose diacetate (CDA), a cost-effective polymer that readily dissolves in acetone or DMF, was selected as the sacrificial polymer for freestanding MOF fabrication. First, a stable metal oxide layer is formed on the fiber surface by ALD, then the polymer is selectively dissolved in acetone solution leaving only the metal oxide hollow structure. The oxide tube is then converted to a hollow MOF by reacting with organic linkers. The process yields hollow fibers with small (~500 nm) diameter suitable for filtration structure, but size and mechanical handling inhibit testing as hollow fiber separator systems. This work further describes the versatility and performance of the

---

[a] Key Laboratory of Textile Science & Technology, Ministry of Education, College of Textiles, Donghua University, Shanghai, 201620, China. Email:kqf@sit.edu.cn
[b] Department of Chemical & Biomolecular Engineering, North Carolina State University, 911 Partners Way, Raleigh, North Carolina 27695, United States. Email:gnp@ncsu.edu
[c] School of Fashion Engineering, Shanghai University of Engineering Science, No.333 Longteng Road, Songjiang, Shanghai, 201620, China

Electronic Supplementary Information (ESI) available: [Detailed experimental procedures; additional information pertaining to SEM and XRD; MOF conversation ratio results; low temperature gas adsorption results; isotherms from IAST simulations; CO_2/N_2 selectivity results (PDF)]. See DOI: 10.1039/x0xx00000x freestanding MIL-53(Al)-NH_2 predominant hollow fiber mats as filters for CO_2 adsorption, CO_2/N_2 separation, and VOC removal. This work is the first to report synthesis of a freestanding MOF fiber with the feature of a hollow structure, and it directly demonstrates a novel and -unique approach to MOF crystal size and pore configuration control which is a common challenge in MOF powder growth._In addition, this study highlights the importance of MOFs in gas separation and VOC heterogeneous catalysis, and may contribute to the design of high performance adsorbents.

Experimental

Materials

Electrospinning polymer: cellulose diacetate (CDA, Eastman Chemicals); **ALD precursor:** diethyl zinc (DEZ, 95% STREM Chemicals Inc.,), trimethyl aluminum (TMA, 98% STREM Chemicals Inc.,); **Metal source:** aluminum chloride hexahydrate ($AlCl_3·6H_2O$, Alfa Aesar), copper nitrate trihydrate ($Cu(NO_3)_2·3H_2O$, 99-104%, Sigma-Aldrich); **Linker:** 2-amino-terephthalic acid (99%, Acros Organics), 2-methylimidazole (99%, Sigma-Aldrich), meso-Tetra (4-carboxyphenyl) porphine (H_2TCPP, >97% Frontier Scientific); **Organic solvent:** acetone (Fisher), N,N-dimethylformamide (DMF, Fisher), N,N-dimethylacetamide (DMAc, 99.8%, Sigma-Aldrich), anhydrous ethanol (200 proof, VWR), were purchased from commercial sources and used without further treatment. Melt-blown polypropylene (PP) fiber mats with density of 40 gsm was used as received from Nonwovens Cooperative Research Center (NCRC), North Carolina State University.

Synthesis of MIL-53(Al)-NH_2 Predominant Hollow Fiber Mats

To synthesize MIL-53(Al)-NH_2 predominant hollow fiber mats, the Al_2O_3@CDA nanofiber mats were first immersed in acetone and heated up to 120 °C for 24 h in a sealed Telfon-lined stainless-steel autoclave reactor to dissolve and remove the CDA polymers. After the heat treatment in acetone, the majority of CDA polymers (~ 90%) were removed from the Al_2O_3@CDA nanofiber mats, which can be calculated by the mass change before and after acetone treatment, leaving the Al_2O_3 hollow fiber mats with tiny polymer residuals. For the conversion of MIL-53(Al)-NH_2 using Al_2O_3 hollow fiber mats as the metal source, 0.106 g 2-amino-terephthalic acid was firstly added to a 20 mL DMF/ water mixture (3/1, v/v), then the mixture was sonicated and stirred for 20 min until complete dissolution. Subsequently, a piece of Al_2O_3 hollow fiber mat (0.030 g) was gently soaked in the prepared solution and transferred into a 100 mL Telfon-lined stainless-steel autoclave reactor. This reactor was then heated at 120 °C for 20 h to finish the solvothermal synthesis. After reaction completed, the as-received MIL-53(Al)-NH_2 hollow fiber mat was washed twice with hot DMF, followed by another 2 times of anhydrous ethanol washing. The MIL-53(Al)-NH_2 hollow fiber mat was finally dried under vacuum at 200 °C for 10 h and stored in before test. As a control group, Al_2O_3@CDA nanofiber mat was also converted into MIL-53(Al)-NH_2 directly using the same recipe mentioned above without the pretreatment in acetone solution. The as-prepared sample was denoted as MIL-53(Al)-NH_2 (CDA).

Characterization

Scanning electron microscopic (SEM) was conducted using a FEI Verios 460 L field emission SEM. X-ray diffraction (XRD) data was collected using a Rigaku SmartLab X-ray diffraction tool (Cu Kα X-ray source) for crystalline structure characterization. X-ray photoelectron spectroscopy (XPS) was performed using a Kratos Analytical Axis Ultra system equipped with an aluminum source (Al Kα = 1486.6 eV radiation). The voltage and current of x-ray gun were 15 kV and 20 mA. All the binding energies were calibrated using the signal from adventitous carbon (C1s = 284.6 eV). In-situ diffuse reflectance infrared fourier transform spectrometry (DRIFTS) was measured on a Fourier transform infrared (FTIR) spectrometer (Model Nicolet 6700, Thermo Fisher, USA). The spectra were recorded with a resolution of 4 cm^{-1} and an accumulation of 64 scans. During HCHO oxidation process, ~80 ppm of HCHO was injected into the DRIFTS cell carried by a synergetic gas (80% N_2, 20% O_2) at a flow rate of 30 mL min^{-1} at room temperature.

Low-pressure Gas Adsorption Measurements

Gas adsorption isotherms in the pressure range of 0-1.1 bar were measured by a volumetric method using a Micromeritics 3Flex Surface Characterization Analyzer. Before analysis, all samples were fully degassed under vacuum at 120 °C for 20 h by using the Smart Vacprep (Micromeritics), a gas adsorption sample preparation device. After the degas process was completed, the sample tubes were weighed and then carefully transferred to the analysis port of the gas adsorption instrument. N_2 adsorption-desorption isotherms at 77 K were measured in liquid nitrogen. N_2 and CO_2 adsorption-desorption isotherms at 273 K were measured using an ice water bath and isotherms at 298 K were measured using water baths. All temperatures were monitored before and after the measurement and no temperature change was detected in all cases.

Thermogravimetric Analysis and CO_2 Cycling Measurement CO_2 cycling experiments were carried out on a TA instruments SDT 650. 15% CO_2/N_2 (Acro) and N_2 (99.999%) were used in this experiment. In a typical test, ~10 mg target sample was loaded into an alumina pan, with a flow rate of 100 mL/min for both gases. The sample was first heated at 100 °C for 40 min under N_2 atmosphere to complete degassing, after the temperature was cooled to 25 °C, MOF sample was swept continuously by CO_2 for 20 min, and then flowing N_2 was maintained for 40 min at 100 °C to activate MOF sample in every cycle. All ramp rates were set as 10 °C/min.

Adsorption and Catalytic Activity Test

The HCHO adsorption and catalytic activities were evaluated in static state using reported proceedures.[33] Specifically, a polytetrafluoroethylene layer stainless steel reactor (0.5 L) was used, at the bottom of which was placed a quartz Petri dish which held the material under test. After putting the dish into the reactor, 300 ppm of HCHO, generated using a S-4000 Gas Mixing system (Environics, USA), was injected into the reactor. After the concentration of HCHO was stabilized to 150 ppm, the cover of the dish was removed to start the adsorption and catalytic reaction of HCHO. HCHO, CO_2, CO and water vapor were recorded online by a photoacoustic IR multigas monitor (INNOVA AirTech Instruments Model 1412i) during test at 25 °C. The yield of CO_2 (ΔCO_2) and the concentration variation of HCHO were calculated to analyze the HCHO removal ratio.

Journal of

Materials Chemistry A

Paper

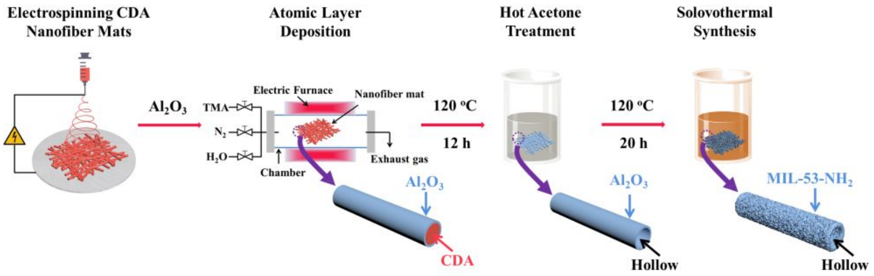

Scheme 1. Schematic illustration of the fabrication of hollow MIL-53(Al)-NH_2 fiber mat. Al_2O_3 hollow fiber mat (obtained from dissolving Al_2O_3@CDA into acetone) was employed as metal source, and was then transferred into the water/DMF mixed solution containing 2-amino-terephthalic acid linkers, which was heated to 120 °C for 20 h.

Results and discussion

Synthesis and Characterization of MIL-53(Al)-NH_2 Hollow Fiber Mats

The procedure developed here for synthesizing freestanding hollow MOFs is shown in **Scheme** 1. Using MIL-53(Al)-NH_2 as an example, the first step was the electrospinning of a CDA nanofiber mat with fiber diameter in the range of 300-500 nm. The as-prepared CDA nanofiber mat was transferred to a lab-made ALD reactor and coated with a conformal metal oxide layer to construct a core-sheath structure (denoted as Al_2O_3@CDA). This Al_2O_3 ALD layer functions as a metal source for MOF structure synthesis by reacting with organic linkers. For most experiments, before MOF synthesis, the Al_2O_3@CDA mat was immersed in acetone at 120 °C for 12 h to dissolve the CDA, yielding an Al_2O_3 hollow fiber mat (**Figure** S1, S2). Then, the hollow Al_2O_3 structure was transferred into solution containing 2-amino-terephthalic acid linkers dissolved in the water/DMF mixed solvent and heated to 120 °C for 20 h. Using this solvothermal synthesis method, the Al_2O_3 hollow structure transformed into MIL-53(Al)-NH_2 and the initial hollow structure was remained intact (**Figure** 1A-B).

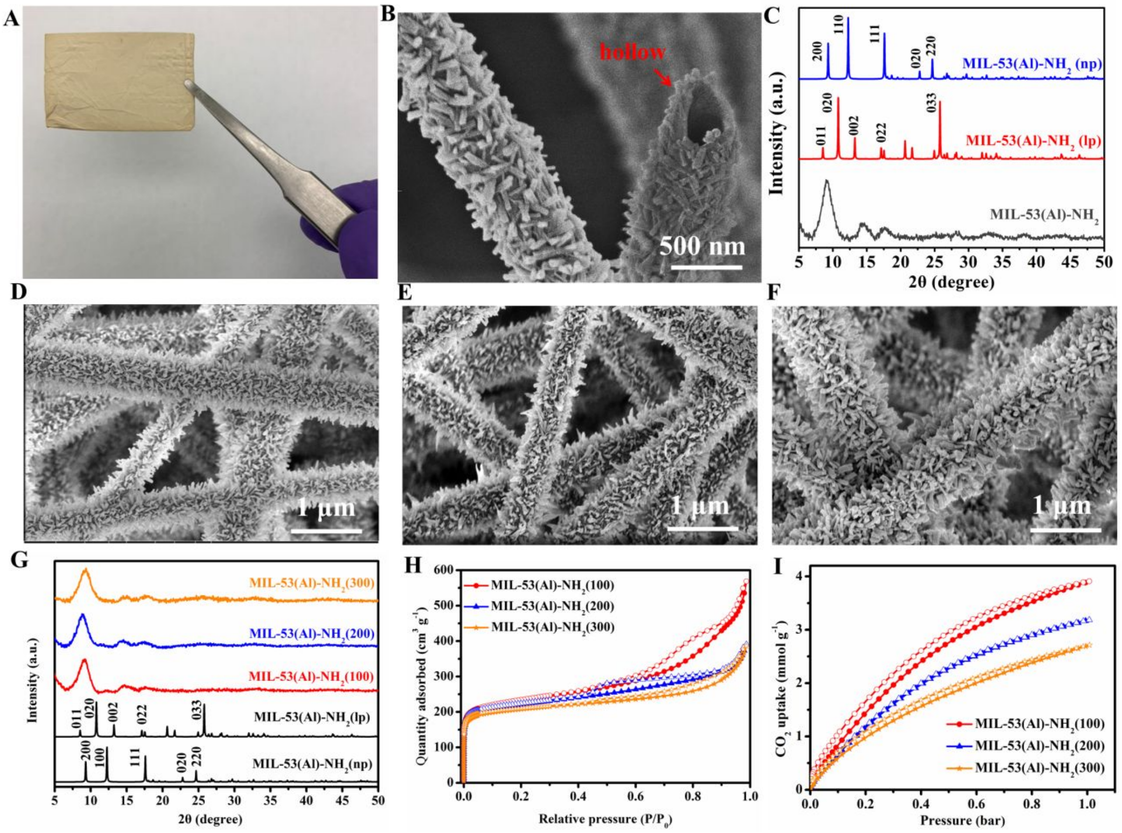

Figure 1. (A) Optical photograph of the freestanding hollow MIL-53(Al)-NH_2. (B) Cross-sectional SEM image of hollow MIL-53(Al)-NH_2 fiber mat. (C) XRD pattern of MIL-53(Al)-NH_2 fiber mat with the simulated patterns for the *lp* and *np* configurations of MIL-53(Al)-NH_2.[36] SEM images of the (D) MIL-53(Al)-NH_2 (100), (E) MIL-53(Al)-NH_2 (200) and (F) MIL-53(Al)-NH_2 (300). Rod-like crystals are observed in all cases, as the ALD layers get thicker, the obtained MOF crystal sizes are increased. (G) XRD pattern of hollow MIL-53(Al)-NH_2 fiber mat fabricated with different ALD thickness. All XRD patterns reveal lp configuration. (H) N_2 isotherms at 77 K. (I) CO_2 isotherms at 273 K

Scanning electron microscopic (SEM) imaging and X-ray diffraction (XRD) confirmed successful formation of MIL-53(Al)-NH_2 hollow fiber mats. As shown in Figure 1B, a rod-like morphology was observed for hollow MIL-53(Al)-NH_2. The MOF crystals with the average size of around 200 nm in length and 5 nm in diameter were conformally formed along the surface of the fiber cylinders. In Figure 1C, the observed characteristic peaks resemble those expected for MOF with large pore (*lp*) configuration although the narrow pore (*np*) structure has been obtained previously for MIL-53(Al)-NH_2 powders.[34, 35]

To obtain the highest quality of hollow MOF fiber mats, systematic experiments were conducted by tuning the thickness of the Al_2O_3 ALD layer. Using 100, 200, and 300 cycles of ALD treatment, that thickness ranges from 12 nm to 40 nm (**Table** S1 and **Figure** S3), denoted as MIL-53(Al)-NH_2 (100), MIL-53(Al)-NH_2 (200), and MIL-53(Al)-NH_2 (300), respectively. By analyzing the results from SEM, XRD, N_2 isotherms, and XPS we found around the 200 cycle sample with thickness of 28 nm was optimal to transform into high quality MOF. As shown in **Figure** 1 (D-F), MIL-53(Al)-NH_2 (100), MIL-53(Al)-NH_2 (200), and MIL-53(Al)-NH_2 (300) exhibit similar morphologies. Moreover, thicker ALD layers tend to produce MOFs with larger crystal size. XRD patterns for the samples prove there is a slight loss on crystallinity as the increase of the ALD layer thickness (**Figure** 1G). In addition, XRD patterns corresponding to *lp* configuration were observed in all MOFs.

High surface area was calculated from N_2 adsorption isotherms at 77 K for the hollow MOF-fibers and the relation between MOF surface area and starting thickness of ALD Al_2O_3 was elucidated. For all hollow MIL-53(Al)-NH_2 fibers, the N_2 adsorption-desorption isotherms at 77 K exhibit slight hysteresis (at higher pressure, $P/P_0 > 0.4$) (**Figure** 1H) reflecting a hierarchical pore structure, involving micro, meso- and macro-poriosity. The MIL-53(Al)-NH_2 crystals contribute to the microporous structure, whereas the spaces between these crystals, hollowness of the fibers, and fibrous mats give rise to meso- and macro-porosity.[22] These meso-macro-porosities with complex pore geometry are consistent with the observed hysteresis in the isotherms, and may lead to capillary condensation at high relative pressure.[37, 38] As shown in **Figure** 1H, the Brunauer-Emmett-Teller (BET) surface area of MIL-53(Al)-NH_2 (100), MIL-53(Al)-NH_2 (200), and MIL-53(Al)-NH_2 (300) is 880 ± 30 m^2 g^{-1}, 842 ± 28 m^2 g^{-1}, and 720 ± 40 m^2 g^{-1}, respectively. The resulting DFT pore diameter distribution curves (Figure S4), show the pore size of all MIL-53(Al)-NH_2 fiber mats are predominantly microporous (0.5–2 nm).[39-41] The textural parameters derived from the N_2 isotherms are included in Table S1.

CO_2 isotherms at 273 K in **Figure 1**I display the same trend of decreasing adsorption capacity on a per-gram basis for hollow MIL-53(Al)-NH_2 materials synthesized with thicker Al_2O_3 layers. Notably, all CO_2 adsorption capacities at 273 K are improved compared to those of MIL-53(Al)-NH_2 powder samples reported,[42, 43] due to more stable *lp* configuration, indicating the great potential of our materials in CO_2 capture or other gas separations.

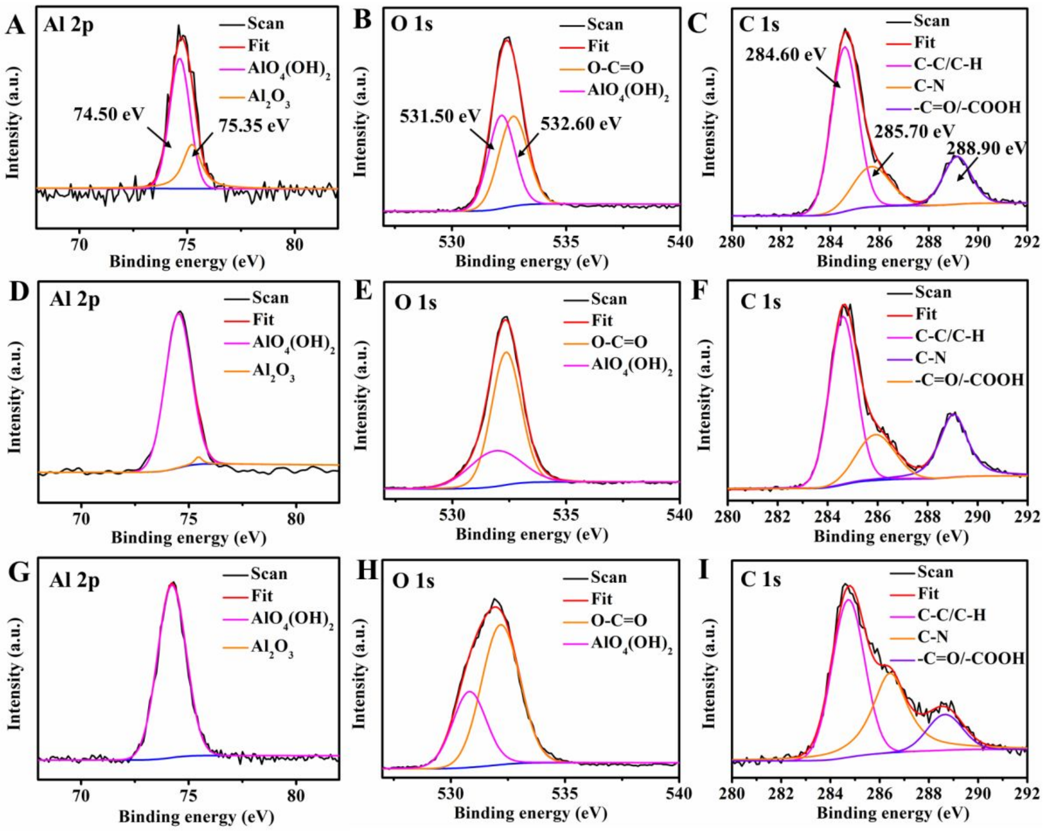

Figure 2. High resolution XPS scans of (A) Al 2p (B) O 1s and (C) C 1s for MIL-53(Al)-NH_2 (300). (D) Al 2p (E) O 1s and (F) C 1s for MIL-53(Al)-NH_2 (200). (G) Al 2p (H) O 1s and (I) C 1s for MIL-53(Al)-NH_2 (100).

Analysis of MOF Conversion Yield

Mass measurements were used to examine MOF quality. The MOF conversion yield was calculated using measured mass, following a procedure adapted from previous reports,[44] and the results are given in Table S1. The yield values given in Table S1 reveal 100% conversion for the thinnest Al_2O_3 layer, with somewhat decreased yield for thicker oxides.

X-ray photoelectron spectroscopy (XPS) analysis was also used to qualitatively confirm the elemental composition of the MOFs. As illustrated in **Figure** 2, the XPS data reflected a similar trend with the mathematical calculation. Two peaks are detected at Al 2p high resolution scan of MIL-53(Al)-NH_2 (300) (**Figure** 2A), where the component at 74.50 eV corresponds to octahedral $AlO_4(OH)_2$ clusters in MOFs, and the component at 75.35 eV is attributed to the unreacted aluminum oxide or byproducts of hydroxide in the hollow structures.

Notably, when thinner Al_2O_3 layers are used, the peak areas for unreacted aluminum oxide at 75.4 eV decrease significantly and no peak is detected for MIL-53(Al)-NH_2 (100) (**Figure** 2G). As observed in the yield calculation, the XPS result also denotes 100% conversion into MIL-53(Al)-NH_2 from Al_2O_3 film with 12 nm thickness. In addition, the O 1s spectra can be divided into two peaks. As shown in **Figure** 2 (B,E,H), the first peak at 531.5 eV is attributed to the coordination of the Al cations with the oxygen anion of the 2-amino-terephthalic acid linker, whereas the latter one at 532.6 eV is assigned to the oxygen in O-C=O. There are three peaks in C 1s emission spectra (**Figure** 2(C,F,I)), which can be assigned to non-oxygenated ring carbon (284.6 eV), C-N bond (285.7 eV), and carboxylate carbon (288.6 eV), respectively.

As shown in **Figure** S5, MIL-53(Al)-NH_2 (200) and MIL-53(Al)-NH_2 (300) form as robust mats, whereas MIL-53(Al)-NH_2 (100) is evidently fragile due to the ultrathin Al_2O_3 shell. In view of structure robustness and MOF quality, MIL-53(Al)-NH_2 (200) was chosen for the application tests. With this information in mind, 200 cycles of ALD Al_2O_3 (i.e. a thickness of 28 nm) is fixed to provide the consumptive metal oxide source in the following experiments.

Growth Mechanism

The mechanism for MOF syntheses from Al_2O_3 proceeds via a dissolution-growth process.[30, 46] In detail, the reaction originates from fast dissolution and hydration of the surface oxide in DMF:Water cosolvent; Al^{3+} species are then generated by the reaction between hydroxylated aluminum and adsorbed H^+ at the near-surface region yielding an aluminum aqua complex ($[Al(H_2O)_6]^{3+}$). Finally, MOF nucleation is promoted by the coordination between aluminum aqua complex and the linkers.[46] However, as the MOF crystal growth consumes the outer Al_2O_3 layer, MOF crystals on the fiber surface can inhibit ligand diffusion into the inner region of the oxide layer,[30] thereby limiting MOF growth.[47, 48]

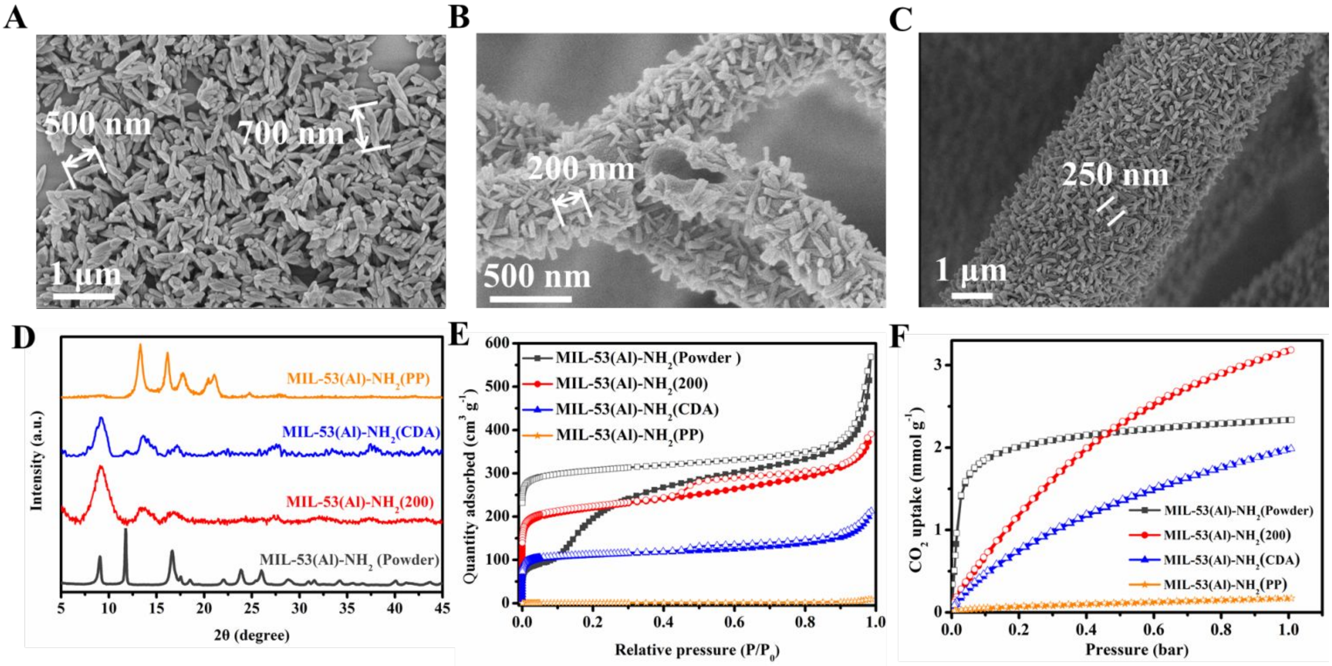

Figure 3. SEM images of the (A) MIL-53(Al)-NH_2 (powder), (B) MIL-53(Al)-NH_2 (CDA) and (C) MIL-53(Al)-NH_2 (PP). MIL-53(Al)-NH_2 converted from metal oxide source given by an ALD process shows a reduced crystal size (D) XRD patterns for MIL-53(Al)-NH_2 materials fabricated by different methods. MIL-53(Al)-NH_2 (200), MIL-53(Al)-NH_2 (CDA) and MIL-53(Al)-NH_2 (PP) can be assigned to *lp* configuration, whereas MIL-53(Al)-NH_2 (powder) is much closer to *np* configuration. (E) N_2 isotherms at 77 K. (F) CO_2 isotherms at 273 K.

Comparison to Powders and Extension to Other Fiber Substrates

We further studied MIL-53(Al)-NH_2 powders produced via solvothermal synthesis, as well as MOF-fibers formed via oxide conversion on cellulose diacetate (CDA) and polypropylene (PP) fibers. The latter materials are referred as MIL-53(Al)-NH_2 (CDA) and MIL-53(Al)-NH_2 (PP), respectively. In these cases, the polymer was not removed before oxide-to-MOF conversion. (**Materials and Synthesis, Supporting Information**). Results of these materials, and comparison to MIL-53(Al)-NH_2 (200) fibers produced with pre-dissolved polymer are shown in **Figure** 3.

As shown in **Figure** 3A, MIL-53(Al)-NH_2 powder samples produced rice-shaped crystals with crystal size in the range of 500-700 nm in length and 80-150 nm in diameter (**Figure** 3A). For the case of MIL-53(Al)-NH_2 (CDA), the SEM image (**Figure** 3B) shows predominantly hollow MOF structure indicating that the CDA polymer scaffold was dissolved during the MOF synthesis. For the MIL-53(Al)-NH_2 (PP), the polymer was not dissolved, yielding a conformally integrated MOF on PP fibers, as shown in **Figure** 3C.

It is also important to note that in contrast to the relatively large MIL-53(Al)-NH_2 crystals produced as powders, the crystals converted from ALD Al_2O_3 on fibers (**Figure** 3B-C) are more well defined and smaller, less than 250 nm in length, which was consistent of the proposed growth mechanism. For all cases, the XRD patterns (**Figure 3**D) of MIL-53(Al)-NH_2 (powder), MIL-53(Al)-NH_2 (CDA), and MIL-53(Al)-NH_2 (PP) show the characteristic peaks, indicating the successful MOF synthesis. The powder samples show features consistent with *np* structure, whereas like the materials shown in **Figure** 1C, the MOF-fibers show spectra consistent with *lp* configuration. The structural changes detected by XRD analysis show flexibility and breathing behavior in the MOFs. The flexibility is expected to arise from the parallel arrangement of the $Al^{III}(OH)(RCOO)_2$ chains and possibly some interpenetrated coordination.[49, 50] This distinction is important as it influences the performance of the MOF-fibers relative to the free MOF powder.

Low-pressure Gas Adsorption Analysis

MIL-53(Al)-NH_2 is known to be flexible with breathing behavior associated with *lp-np* transitions even at room temperature. The breathing behavior for MIL-53(Al)-NH_2 powders can be triggered by various gases such as CO_2, CH_4, and C_2H_6.[51] Kitagawa and coworkers described a close relationship between MOF crystal size and the framework flexibility; that is, nanometer-scale crystals provide stability to the pore configuration in a flexible MOF structure, resulting in a thermodynamic and/or kinetic suppression in pores transition.[25, 52] Therefore, the smaller 200 nm *lp* dominated MIL-53(Al)-NH_2 (200) MOFs are expected to possess much more stable pore configuration and be restricted further from breathing.

N_2 adsorption-desorption isotherms (**Figure** 3E) confirm the hypothesis that MIL-53(Al)-NH_2 (200) features much more stable pore structures than the powder phase. For MIL-53(Al)-NH_2 (powder), it shows *np* configuration in room temperature, and the *np-lp* transition is evidently triggered at 120°C by the degassing process.[53, 54] In **Figure** 3E, the N_2 adsorption isotherm at 77 K for MIL-53(Al)-NH_2 (powder) shows two plateaus, one at around 0.02-0.1 P P_0^{-1} associated with *lp-np* transition, and another at 0.4-0.6 P P_0^{-1} associated with *np-lp* transition.[55, 56]

In separate tests, hollow MOF-fibers were produced from Al_2O_3 ALD layers either before or after removing the CDA fiber substrate. Removing the polymer before oxide-to-MOF conversion led to N_2 isotherms with a much more stable pore configuration and BET surface area of 842 ± 28 m^2 g^{-1}. This surface area is ~ 2x larger than 480 ± 21 m^2 g^{-1} measured for MIL-53(Al)-NH_2 formed with the CDA not removed before oxide to MOF conversion. The small surface area for MOFs formed before polymer removal is ascribed to infusion of dissolved CDA into the MOF to partly block the pore volume (**Table** S1). This highlights the significance of the pre-dissolution treatment in formation of a hollow structure MOF with less impurities and higher crystallinity. The pore size distribution results indicate the MIL-53(Al)-NH_2 powder and MIL-53(Al)-NH_2-PP fiber show hierarchical pore structure, whereas the MIL-53(Al)-NH_2 (CDA) fiber only show microporous structure (**Figure S**6).[39-41]

From the CO_2 isotherms, it can be observed that MIL-53(Al)-NH_2 (200) spans a higher range at a relative pressure at 0.4 bar over MIL-53(Al)-NH_2 (powder) isotherm, exhibiting a more stable pore configuration and higher CO_2 uptake (**Figure** 3F). That is because, after the *lp-np* transition at 0-0.1 bar, the MIL-53(Al)-NH_2 (powder) still forms in the *np* phase, and is unable to have additional gas uptake. In comparison, MIL-53(Al)-NH_2 (200) is stabilized in the *lp* phase and has continued adsorption throughout this region.[53, 54]

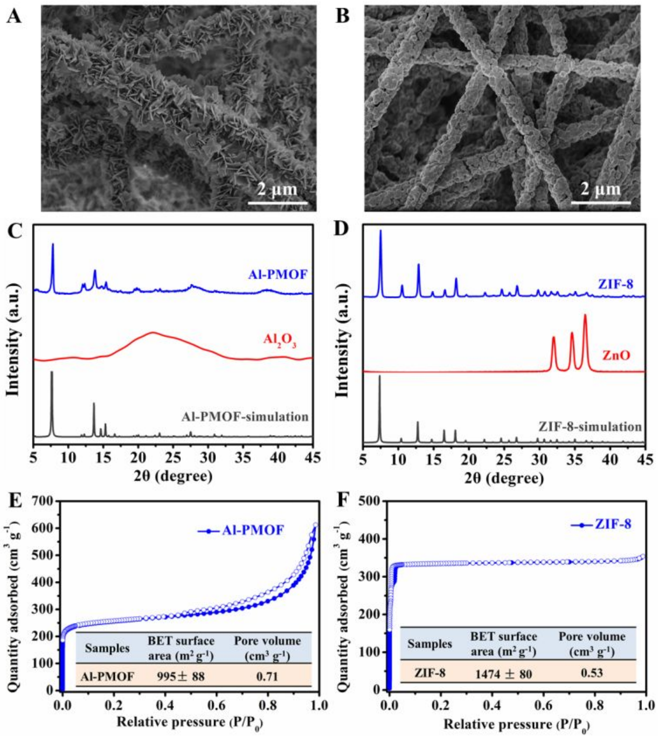

Figure 4. SEM images of the (A) Al-PMOF predominant fiber mat, (B) ZIF-8 predominant fiber mat. Freestanding fiber structures are remained from their parent phases of Al_2O_3 and ZnO nanofibers, respectively. XRD patterns of (C) Al-PMOF and (D) ZIF-8. It confirms that both Al-PMOF and ZIF-8 have been converted successfully and the characteristic peaks are identical with the simulation patterns. N_2 isotherms for (E) Al-PMOF and (F) ZIF-8 at 77K. Inset shows the decent BET surface areas and pore volumes of Al-PMOF and ZIF-8.

Furthermore, among the four samples studied, the MIL-53(Al)-NH_2 (200) shows the highest CO_2 uptake at 1 bar, reaching to 3.30 ± 0.07 mmol g^{-1} (**Table S**1) which is significantly higher than that reported in previous studies.[42, 57]

Extension to Other MOF Materials

To confirm that our synthetic approach can be extended to other materials, we synthesized other hollow MOF fibers including Zn and Al based structures (**Methods, Supporting information**). **Figure** 4 shows Al-PMOF and ZIF-8 structures formed by transforming from Al_2O_3 hollow structure, yielding freestanding MOF predominant nanofiber mats. The SEM images, XRD patterns, and N_2 adsorption-desorption isotherms (**Figure** 4) confirm successful fabrication of the MOF structure.

Potential Applications on MIL-53(Al)-NH_2 Hollow Fiber Mats

The performance of the MIL-53(Al)-NH_2 fiber mats and powders were evaluated in gas separation and VOC removal applications. Over the past decade, experimental and computational analysis show promising potential for MOFs in CO_2 capture [58-60] and CO_2/N_2 and CO_2/CH_4 separation.[49,61,62] For the MIL-53(Al)-NH_2 hollow fibers samples produced here, volumetric gas adsorption analysis shown in **Figure** 3F confirm high CO_2 adsorption capacities, showing promise for advanced application.

To analyze CO_2/N_2 selectivity, we applied the ideal adsorbed solution theory (IAST) using adsorption data of single-component gases (**Table** S2, **Figure** S7-S10).[63-68] As shown in **Figure** 5, the MIL-53(Al)-NH_2 (200) material shows a moderate CO_2/N_2 selectivity. The values of IAST selectivity at 273 K and 1 bar for 15/85 and 50/50 CO_2/N_2 mixtures are about 24.9 and 21.2, respectively. It should be pointed out that the MIL-53(Al)-NH_2 (200) shows much lower selectivity compared with MIL-53(Al)-NH_2 (powder) (**Figure** S11). We attribute this to the inherent low N_2 uptake on powders, which results in ultrahigh CO_2/N_2 selectivity on MIL-53(Al)-NH_2 (powder) both at 15/85 and 50/50 CO_2/N_2 mixture at 1 bar.

The CO_2/N_2 selectivity is further confirmed by binary gas-adsorption experiment via a gravimetric method, where the CO_2/N_2 mixture (15/85) is utilized to simulate the major components of flue gas. As shown in **Figure** 6A, no apparent capacity loss is observed after 21 cycles with a mass change of 4.5%, indicating that the MIL-53(Al)-NH$_2$ (200) is capable withstanding cyclic exposure to the gas mixture and able to remove CO_2 from flue gases.

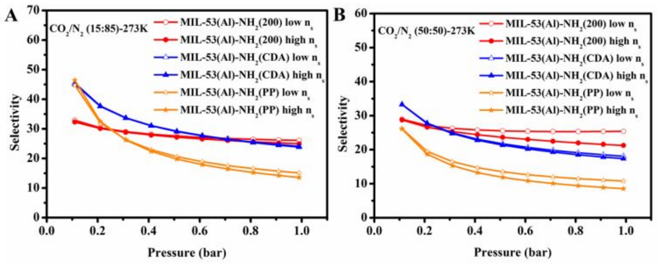

Figure 5. Selectivity by the IAST calculations at 273 K with CO_2 and N_2 molar ratio of (A) 15/85 and (B) 50/50 in the gas phase.

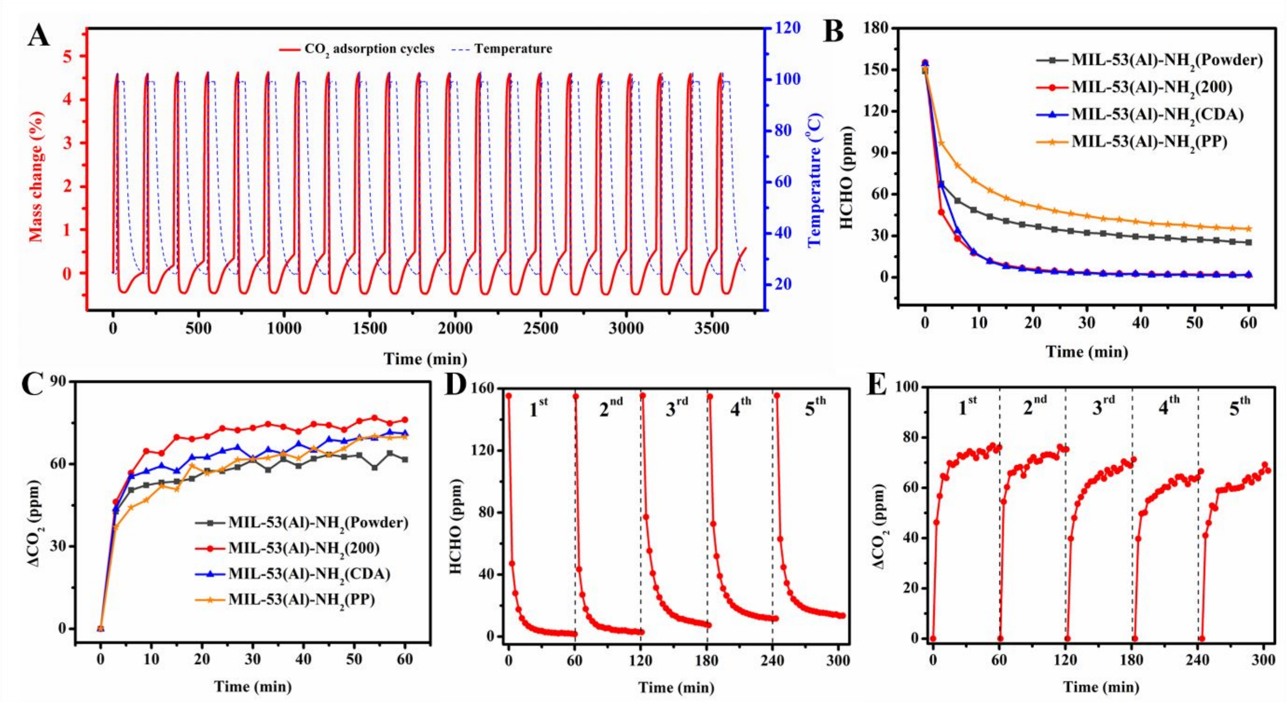

Figure 6. (A) Cyclic CO_2 adsorption behavior measured by thermogravimetric method with introducing a 15% CO_2 mixture in N_2 at 25 °C. The initial mass was normalized to 0% at 25 °C under N_2 atmosphere. HCHO removal tests over MIL-53(Al)-NH$_2$ (powder), MIL-53(Al)-NH$_2$ (200), MIL-53(Al)-NH$_2$ (CDA) and MIL-53(Al)-NH$_2$ (PP): variation of the concentration of (B) HCHO; (C) CO_2. Reproducibility tests of HCHO removal performance on MIL-53(Al)-NH$_2$ (200): variation of the concentration of (D) HCHO; (E) CO_2. (F) Proposed heterogeneous catalytic mechanism in HCHO removal using MIL-53(Al)-NH$_2$ (200) as a catalyst.

Beyond application in gas separation, MIL-53(Al)-NH$_2$ hollow fibers produced under several conditions were further investigated for their catalytic activity for VOC formaldehyde (HCHO) oxidation.[69-72] Results were compared to that of the MIL-53(Al)-NH$_2$ powder. HCHO removal performance was measured statically in an airtight reactor, with samples cyclically and automatically taken at 1 minute intervals and monitored by utilizing a photoacoustic IR multigas monitor for appearance of CO_2 and decrease of HCHO.[72] The data clearly indicates a heterogeneous removal of HCHO [69-71] on each MIL-53(Al)-NH$_2$ sample. The adsorption-degradation-desorption process active in this system produces the expected HCHO reduction and CO_2 generation (**Figure** 6B-C).[70] The catalytic activity performance is determined by the variation of HCHO concentration after 60 min (**Figure** 6B). Results confirm that the MIL-53(Al)-NH$_2$ (200) with the hollow structure shows the best HCHO catalytic activity, followed by MIL-53(Al)-NH$_2$ (CDA), MIL-53(Al)-NH$_2$ (powder) and MIL-53(Al)-NH$_2$ (PP). The superior performance of MIL-53(Al)-NH$_2$ (200) is ascribed to the unique hollow fiber structure. In part, the radial growth of MOF crystals along with fiber cylinders can diminish most aggregation effects seen in the powder phase. The hollow structure facilitates HCHO molecule flow into the inner side of the cylinders, thereby encountering more active sites. It is worth noting that the MIL-53(Al)-NH$_2$ (200) exhibits excellent reproducibility in HCHO removal analysis, even with a tiny dosage (ca. 35 mg), and still retain the HCHO removal ability of around 92.9% after 5 cyclic tests (**Figure** 6D-E). Moreover, the morphology of the MIL-53(Al)-NH$_2$ (200) fiber mats remains intact after HCHO removal testing (**Figure S**12), indicating good stability of the MOF structure. The VOC removal performance of selected MOFs is summarized in

Table S3. In comparison with other MOFs, the MIL-53(Al)-NH_2 (200) shows competative performance in overall VOC removal.

To demonstrate the degradation pathway of HCHO on MIL-53(Al)-NH_2 (200), in-situ observation of DRIFTS spectra exposed to a flow of ~80 ppm HCHO/synthetic air within 30 min was recorded at room temperature. As shown in **Figure** 7A, characteristic peaks around 1728 cm^{-1}, 3346 cm^{-1}, 3419 cm^{-1}, and 3579 cm^{-1} can be ascribed to gas HCHO (National Institute of Standards and Technology (NIST) Standard Reference Database 69), indicating the quick adsorption by the porous MOF structure. The formation of formate species (1570 cm^{-1}, 2903 cm^{-1}), and carbonate species (1266 cm^{-1}) can be clearly observed on the spectra, revealing that the formate species are the main intermediates during the HCHO oxidation process. [73,74] The negative signals around 3657 cm^{-1} can be assigned to surface hydroxyl groups. Based on the results, the proposed mechanism of HCHO removal on MIL-53(Al)-NH_2 (200) is illustrated in **Figure** 7B. The heterogeneous catalytic process is composed by several intermediate details. In detail, HCHO molecules are adsorbed by the porous structures initially and then oxidized by $AlO_4(OH)_2$ clusters to transform to formate and carbonate species, finally degrade to harmless products of CO_2 and H_2O.

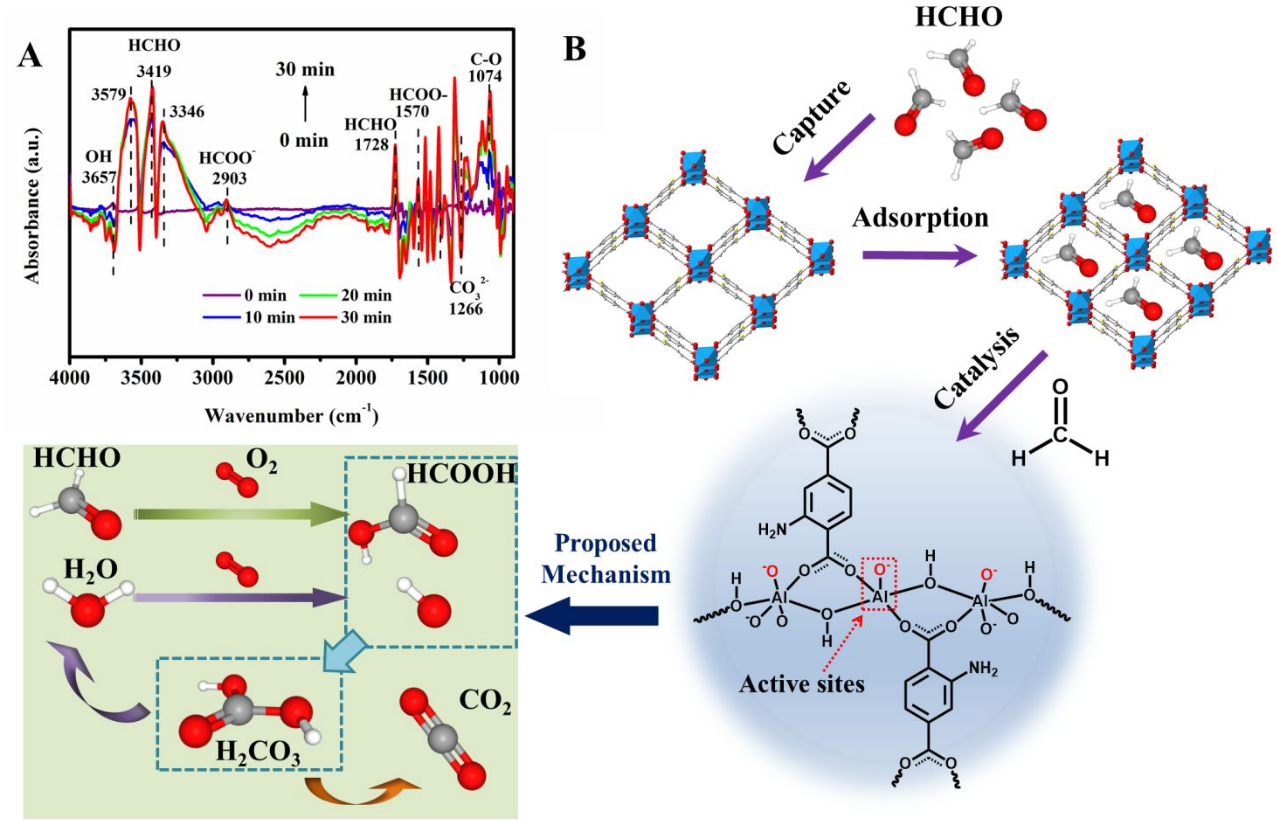

Figure 7. (A) In situ DRIFTS spectra of MIL-53(Al)-NH_2 (200) exposed to a flow of ~80 ppm of HCHO/synergetic air at room temperature. (B) Proposed heterogeneous catalytic mechanism in HCHO removal using MIL-53(Al)-NH_2 (200) as a catalyst.

Conclusions

This work demonstrates a novel approach to fabricate free-standing MIL-53(Al)-NH_2 fiber mats in a unique hollow structure with high crystallinity and porosity. The method can also be extended to other MOF systems with freestanding hollow structure. The freestanding MOF-fiber mat converted from metal oxide source formed by ALD shows well controlled crystal size and more stable pore configuration as well as a restrained breathing behavior in a flexible MOF structure compared with its powder phase. Experimental analysis confirms that predominant MIL-53(Al)-NH_2 hollow fiber mats have promising potential in CO_2 adsorption, CO_2/N_2 separation, and VOC abatement applications.

Conflicts of interest

"There are no conflicts to declare".

Acknowledgements

Part of this work was performed at the Analytical Instrumentation Facility (AIF) at North Carolina State University, which is supported by the State of North Carolina and the National Science Foundation (award number ECCS-1542015). The AIF is a member of the North Carolina Research Triangle Nanotechnology Network (RTNN), a site in the National Nanotechnology Coordinated Infrastructure (NNCI). GNP acknowledges support from the U.S. National Science Foundation, Award No. 1704151. Z.D. acknowledges China Scholarship Council (CSC) from the Ministry of Education of P.R. China for two-year financial support of studying at North Carolina State University (File No. 201706630121). Z.D. acknowledges support from the Fundamental Research Funds for the Central Universities (No. CUSF-DH-D-2017010). We thank Professor Saad Khan for the use of electrospinning setup. We thank Seung Keun Song and Jungsik Kim for XPS measurements and Jiafei Su from Shanghai Normal University for the measurement of HCHO catalytic activity test.

Notes and references

[1] H. Li, M. Eddaoudi, M. O'Keeffe and O. M. Yaghi, *Nature*, 1999, **402**, 276-279.

[2] L. F. Chen and Q. Xu, *Science*, 2017, **358**, 304-305.

[3] T. Rodenas, I. Luz, G. Prieto, B. Seoane, H. Miro, A. Corma, F. Kapteijn, F. Xamena and J. Gascon, *Nature Materials*, 2015, **14**, 48-55.

[4] H. Furukawa, K. E. Cordova, M. O'Keeffe and O. M. Yaghi, *Science*, 2013, **341**, 1230444.

[5] X. D. Zhang, Y. Yang, L. Song, J. F. Chen, Y. Q. Yang and Y. X. Wang, *Journal of Hazardous Materials*, 2019, **365**, 597-605.

[6] X. D. Zhang, Y. Yang, X. T. Lv, Y. X. Wang, N. Liu, D. Chen and L. F. Cui, *Journal of Hazardous Materials*, 2019, **366**, 140-150.

[7] X. D. Zhang, X. T. Lv, X. Y. Shi, Y. Yang and Y. Q. Yang, *Journal of Colloid and Interface Science*, 2019, **539**, 152-160.

[8] X. D. Zhang, Y. Yang, W. Y. Huang, Y. Q. Yang, Y. X. Wang, C. He, N. Liu, M. H. Wu and L. Tang, *Materials Research Bulletin*, 2018, **99**, 349-358.

[9] N. Liu, W. Y. Huang, M. Q. Tang, C. C. Yin, B. Gao, Z. M. Li, L. Tang, J. Q. Lei, L. F. Cui and X. D. Zhang, *Chemical Engineering Journal*, 2019, **359**, 254-264.

[10] X. Zhang, X. Lv, F. Bi, G. Lu and Y. Wang, *Molecular Catalysis*, 2019, DOI: https://doi.org/10.1016/j.mcat.2019.110701, 110701.

[11] X. D. Zhang, X. L. Zhang, L. Song, F. L. Hou, Y. Q. Yang, Y. X. Wang and N. Liu, *International Journal of Hydrogen Energy*, 2018, **43**, 18279-18288.

[12] Y. Q. Yang, H. Dong, Y. Wang, C. He, Y. X. Wang and X. D. Zhang, *Journal of Solid State Chemistry*, 2018, **258**, 582-587.

[13] X. D. Zhang, Y. Yang, L. Song, Y. X. Wang, C. He, Z. Wang and L. F. Cui, *Molecular Catalysis*, 2018, **447**, 80-89.

[14] X. D. Zhang, F. L. Hou, Y. Yang, Y. X. Wang, N. Liu, D. Chen and Y. Q. Yang, *Applied Surface Science*, 2017, **423**, 771-779.

[15] Y. Wang, Y. Q. Yang, N. Liu, Y. X. Wang and X. D. Zhang, *RSC Advances*, 2018, **8**, 33096-33102.

[16] X. J. Ma, Y. T. Chai, P. Li and B. Wang, *Accounts of Chemical Research*, 2019, **52**, 1461-1470.

[17] Y. F. Chen, S. H. Zhang, S. J. Cao, S. Q. Li, F. Chen, S. Yuan, C. Xu, J. W. Zhou, X. Feng, X. J. Ma and B. Wang, *Advanced Materials*, 2017, **29**.

[18] J. J. Zhao, D. T. Lee, R. W. Yaga, M. G. Hall, H. F. Barton, I. R. Woodward, C. J. Oldham, H. J. Walls, G. W. Peterson and G. N. Parsons, *Angewandte Chemie-International Edition*, 2016, **55**, 13224-13228.

[19] D. T. Lee, J. J. Zhao, G. W. Peterson and G. N. Parsons, *Chemistry of Materials*, 2017, **29**, 4894-4903.

[20] X. L. Ma, P. Kumar, N. Mittal, A. Khlyustova, P. Daoutidis, K. A. Mkhoyan and M. Tsapatsis, *Science*, 2018, **361**, 1008-1011.

[21] S. L. Qiu, M. Xue and G. S. Zhu, *Chemical Society Reviews*, 2014, **43**, 6116-6140.

[22] D. T. Lee, J. D. Jamir, G. W. Peterson and G. N. Parsons, *Small*, 2019, **15**, 1805133.

[23] Y. Y. Zhang, S. Yuan, X. Feng, H. W. Li, J. W. Zhou and B. Wang, *Journal of the American Chemical Society*, 2016, **138**, 5785-5788.

[24] Y. C. Lin, C. L. Kong, Q. J. Zhang and L. Chen, *Advanced Energy Materials*, 2017, **7**.

[25] A. Pustovarenko, M. G. Goesten, S. Sachdeva, M. X. Shan, Z. Amghouz, Y. Belmabkhout, A. Dikhtiarenko, T. Rodenas, D. Keskin, I. K. Voets, B. M. Weckhuysen, M. Eddaoudi, L. de Smet, E. J. R. Sudholter, F. Kapteijn, B. Seoane and J. Gascon, *Advanced Materials*, 2018, **30**.

[26] H. X. Liang, X. L. Jiao, C. Li and D. R. Chen, *Journal of Materials Chemistry A*, 2018, **6**, 334-341.

[27] P. Horcajada, R. Gref, T. Baati, P. K. Allan, G. Maurin, P. Couvreur, G. Ferey, R. E. Morris and C. Serre, *Chemical Reviews*, 2012, **112**, 1232-1268.

[28] H. X. Liang, A. N. Yao, X. L. Jiao, C. Li and D. R. Chen, *ACS Applied Materials & Interfaces*, 2018, **10**, 20396-20403.

[29] D. B. Dwyer, D. T. Lee, S. Boyer, W. E. Bernier, G. N. Parsons and W. E. Jones, *ACS Applied Materials & Interfaces*, 2018, **10**, 25794-25803.

[30] J. Reboul, S. Furukawa, N. Horike, M. Tsotsalas, K. Hirai, H. Uehara, M. Kondo, N. Louvain, O. Sakata and S. Kitagawa, *Nature Materials*, 2012, **11**, 717-723.

[31] K. Khaletskaya, S. Turner, M. Tu, S. Wannapaiboon, A. Schneemann, R. Meyer, A. Ludwig, G. Van Tendeloo and R. A. Fischer, *Advanced Functional Materials*, 2014, **24**, 4804-4811.

[32] J. J. Zhao, M. D. Losego, P. C. Lemaire, P. S. Williams, B. Gong, S. E. Atanasov, T. M. Blevins, C. J. Oldham, H. J. Walls, S. D. Shepherd, M. A. Browe, G. W. Peterson and G. N. Parsons, *Advanced Materials Interfaces*, 2014, **1**, 1400040.

[33] Z. J. Dai, X. W. Yu, C. Huang, M. Li, J. F. Su, Y. P. Guo, H. Xu and Q. F. Ke, *RSC Advances*, 2016, **6**, 97022-97029.

[34] A. Boutin, S. Couck, F. X. Coudert, P. Serra-Crespo, J. Gascon, F. Kapteijn, A. H. Fuchs and J. F. M. Denayer, *Microporous and Mesoporous Materials*, 2011, **140**, 108-113.

[35] S. Couck, E. Gobechiya, C. E. A. Kirschhock, P. Serra-Crespo, J. Juan-Alcaniz, A. M. Joaristi, E. Stavitski, J. Gascon, F. Kapteijn, G. V. Baron and J. F. M. Denayer, *Chemsuschem*, 2012, **5**, 740-750.

[36] N. Alvarez-Gutierrez, M. V. Gil, F. Rubiera and C. Pevida, *Fuel Processing Technology*, 2016, **142**, 361-369.

[37] A. Corma, V. Fornes, S. B. Pergher, T. L. M. Maesen and J. G. Buglass, Nature, 1998, 396, 353-356.

[38] M. Choi, K. Na, J. Kim, Y. Sakamoto, O. Terasaki and R. Ryoo, *Nature*, 2009, **461**, 246-249.

[39] X. D. Zhang, H. X. Li, X. T. Lv, J. C. Xu, Y. X. Wang, C. He, N. Liu, Y. Q. Yang and Y. Wang, *Chemistry-a European Journal*, 2018, **24**, 8822-8832.

[40] X. D. Zhang, H. X. Li, F. L. Hou, Y. Yang, H. Dong, N. Liu, Y. X. Wang and L. F. Cui, *Applied Surface Science*, 2017, **411**, 27-33.

[41] X. D. Zhang, F. L. Hou, H. X. Li, Y. Yang, Y. X. Wang, N. Liu and Y. Q. Yang, *Microporous and Mesoporous Materials*, 2018, **259**, 211-219.

[42] P. Serra-Crespo, E. Gobechiya, E. V. Ramos-Fernandez, J. Juan-Alcaniz, A. Martinez-Joaristi, E. Stavitski, C. E. A.

Kirschhock, J. A. Martens, F. Kapteijn and J. Gascon, *Langmuir*, 2012, **28**, 12916-12922.

[43] H. R. Abid, Z. H. Rada, X. Duan, H. Sun and S. Wang, *Energy & Fuels*, 2018, **32**, 4502-4510.

[44] M. Bechelany, M. Drobek, C. Vallicari, A. Abou Chaaya, A. Julbe and P. Miele, *Nanoscale*, 2015, **7**, 5794-5802.

[45] C. M. Moran, J. N. Joshi, R. M. Marti, S. E. Hayes and K. S. Walton, *Journal of the American Chemical Society*, 2018, **140**, 9148-9153.

[46] H. Robatjazi, D. Weinberg, D. F. Swearer, C. Jacobson, M. Zhang, S. Tian, L. N. Zhou, P. Nordlander and N. J. Halas, *Science Advances*, 2019, **5**.

[47] K. Okada, R. Ricco, Y. Tokudome, M. J. Styles, A. J. Hill, M. Takahashi and P. Falcaro, *Advanced Functional Materials*, 2014, **24**, 1969-1977.

[48] J. Cravillon, R. Nayuk, S. Springer, A. Feldhoff, K. Huber and M. Wiebcke, *Chemistry of Materials*, 2011, **23**, 2130-2141.

[49] E. J. Carrington, C. A. McAnally, A. J. Fletcher, S. P. Thompson, M. Warren and L. Brammer, *Nature Chemistry*, 2017, **9**, 882-889.

[50] S. B. Choi, H. Furukawa, H. J. Nam, D.-Y. Jung, Y. H. Jhon, A. Walton, D. Book, M. O'Keeffe, O. M. Yaghi and J. Kim, *Angewandte Chemie International Edition*, 2012, 51, 8791-8795.

[51] L. Bolinois, T. Kundu, X. R. Wang, Y. X. Wang, Z. G. Hu, K. Koh and D. Zhao, *Chemical Communications*, 2017, **53**, 8118-8121.

[52] Y. Sakata, S. Furukawa, M. Kondo, K. Hirai, N. Horike, Y. Takashima, H. Uehara, N. Louvain, M. Meilikhov, T. Tsuruoka, S. Isoda, W. Kosaka, O. Sakata and S. Kitagawa, *Science*, 2013, **339**, 193-196.

[53] W. P. Mounfield and K. S. Walton, *Journal of Colloid and Interface Science*, 2015, **447**, 33-39.

[54] A. Boutin, F. X. Coudert, M. A. Springuel-Huet, A. V. Neimark, G. Ferey and A. H. Fuchs, *Journal of Physical Chemistry C*, 2010, **114**, 22237-22244.

[55] T. Ahnfeldt, D. Gunzelmann, T. Loiseau, D. Hirsemann, J. Senker, G. Ferey and N. Stock, *Inorganic Chemistry*, 2009, **48**, 3057-3064.

[56] T. Lescouet, E. Kockrick, G. Bergeret, M. Pera-Titus, S. Aguado and D. Farrusseng, *Journal of Materials Chemistry*, 2012, **22**, 10287-10293.

[57] F. Zhang, X. Q. Zou, X. Gao, S. J. Fan, F. X. Sun, H. Ren and G. S. Zhu, *Advanced Functional Materials*, 2012, **22**, 3583-3590.

[58] K. Sumida, D. L. Rogow, J. A. Mason, T. M. McDonald, E. D. Bloch, Z. R. Herm, T. H. Bae and J. R. Long, *Chemical Reviews*, 2012, **112**, 724-781.

[59] A. O. Yazaydin, R. Q. Snurr, T. H. Park, K. Koh, J. Liu, M. D. LeVan, A. I. Benin, P. Jakubczak, M. Lanuza, D. B. Galloway, J. J. Low and R. R. Willis, *Journal of the American Chemical Society*, 2009, **131**, 18198

[60] J. M. Yu, L. H. Xie, J. R. Li, Y. G. Ma, J. M. Seminario and P. B. Balbuena, *Chemical Reviews*, 2017, **117**, 9674-9754.

[61] J. R. Li, J. M. Yu, W. G. Lu, L. B. Sun, J. Sculley, P. B. Balbuena and H. C. Zhou, *Nature Communications*, 2013, **4**.

[62] M. Wriedt, J. P. Sculley, A. A. Yakovenko, Y. G. Ma, G. J. Halder, P. B. Balbuena and H. C. Zhou, *Angewandte Chemie-International Edition*, 2012, **51**, 9804-9808.

[63] A. L. Myers and J. M. Prausnitz, *Aiche Journal*, 1965, **11**, 121.

[64] J. A. Mason, K. Sumida, Z. R. Herm, R. Krishna and J. R. Long, *Energy & Environmental Science*, 2011, **4**, 3030-3040.

[65] T. M. McDonald, D. M. D'Alessandro, R. Krishna and J. R. Long, *Chemical Science*, 2011, **2**, 2022-2028.

[66] R. Sips, *Journal of Chemical Physics*, 1948, **16**, 490-495.

[67] D.D. Do, Adsorption Analysis: Equilibria and Kinetics, **1998**. doi:10.1142/p111.

[68] K. H. Shi, E. E. Santiso and K. E. Gubbins, *Langmuir*, 2019, **35**, 5975-5986.

[69] J. L. Wang, J. Li, P. Y. Zhang and G. K. Zhang, *Applied Catalysis B-Environmental*, 2018, **224**, 863-870.

[70] S. Rong, P. Zhang, F. Liu and Y. Yang, *ACS Catalysis*, 2018, **8**, 3435-3446.

[71] J. Q. Torres, S. Royer, J. P. Bellat, J. M. Giraudon and J. F. Lamonier, *Chemsuschem*, 2013, **6**, 578-592.

[72] Z. J. Dai, J. F. Su, X. M. Zhu, K. L. Xu, J. Zhu, C. Huang and Q. F. Ke, *Journal of Materials Chemistry A*, 2018, **6**, 14856-14866.

[73] L. Zhu, J. L. Wang, S. P. Rong, H. Y. Wang and P. Y. Zhang, *Applied Catalysis B-Environmental*, 2017, **211**, 212-221.

[74] F. Liu, S. P. Rong, P. Y. Zhang and L. L. Gao, *Applied Catalysis B-Environmental*, 2018, **235**, 158-167.